Orientation-Dependent Mechanical Responses and Plastic Deformation Mechanisms of FeMnCoCrNi High-entropy Alloy: A Molecular Dynamics Study

Hai-Feng Zhang[1] · **Hai-Le Yan**[1] · **Feng Fang**[2] · **Nan Jia**[1]

Abstract

Mechanical properties of high-entropy alloys (HEAs) with the face-centered cubic (fcc) structure strongly depend on their initial grain orientations. However, the orientation-dependent mechanical responses and the underlying plastic flow mechanisms of such alloys are not yet well understood. Here, deformation of the equiatomic FeMnCoCrNi HEA with various initial orientations under uniaxial tensile testing has been studied by using atomistic simulations, showing the results consistent with the recent experiments on fcc HEAs. The quantitative analysis of the activated deformation modes shows that the initiation of stacking faults is the main plastic deformation mechanism for the crystals initially oriented with [001], [111], and [112], and the total dislocation densities in these crystals are higher than that with the [110] and [123] orientations. Stacking faults, twinning, and hcp-martensitic transformation jointly promote the plastic deformation of the [110] orientation, and twinning in this crystal is more significant than that with other orientations. Deformation in the crystal oriented with [123] is dominated by the hcp-martensite transformation. Comparison of the mechanical behaviors in the FeMnCoCrNi alloy and the conventional materials, i.e. Cu and $Fe_{50}Ni_{50}$, has shown that dislocation slip tends to be activated more readily in the HEA. This is attributed to the larger lattice distortion in the HEA than the low-entropy materials, leading to the lower critical stress for dislocation nucleation and elastic–plastic transition in the former. In addition, the FeMnCoCrNi HEA with the larger lattice distortion leads to an enhanced capacity of storing dislocations. However, for the [001]-oriented HEA in which dislocation slip and stacking fault are the dominant deformation mechanisms, the limited deformation modes activated are insufficient to improve the work hardening ability of the material.

Keywords High-entropy alloy · Molecular dynamics study · Mechanical response · Plastic deformation mechanism

✉ Hai-Le Yan
  yanhaile@mail.neu.edu.cn

✉ Nan Jia
  jian@atm.neu.edu.cn

1 Key Laboratory for Anisotropy and Texture of Materials (Ministry of Education), School of Material Science and Engineering, Northeastern University, Shenyang 110819, China

2 State Key Lab Rolling & Automat, Northeastern University, Shenyang 110819, China

1 Introduction

Based on the design concept of multi-principal-element alloys, high-entropy alloys (HEAs) have attracted great research attention in the fields of materials and physics [1–11]. Compared with traditional metals and alloys, HEAs exhibit four effects including high entropy effect in thermodynamics, hysteresis diffusion effect in kinetics, lattice distortion effect in crystallography, and cocktail effect that are applicable in alloy design [3, 4, 12–16].

Numerous studies have shown that HEAs with the face-centered cubic (fcc) structure exhibit excellent mechanical properties during plastic deformation, i.e., the good combination of high strength and good plasticity [6, 8, 16]. Medium- and high-entropy alloys composed of 3d transition metal elements are usually single-phase or dual-phase solid solutions in which the fcc austenite is the dominating

phase, such as CoCrNi [11, 17–20], CoVNi [16], FeCoCrNi [21], FeMnCoCr [8, 22–25] and FeMnCoCrNi [6, 26–30] alloys. Among them, the equiatomic FeMnCoCrNi alloy, also known as the Cantor alloy [2], is the earliest studied and the most representative fcc-structured HEA. Experimental studies have shown that compared with the 293 K condition, the yield and the ultimate tensile strength of the Cantor alloy with an average grain size of ~ 6 μm increase by 389 and 530 MPa at 77 K, respectively, while the uniform elongation increases by 16%. The simultaneous enhancement in strength and plasticity under cryogenic condition is attributed to the activation of mechanical nano-twinning [6]. Since the plastic deformation mechanism depends on the stacking fault energy (SFE), special attention has been paid to the SFE of this alloy. With the exact muffin-tin orbitals (EMTO) method, the SFE of the Cantor alloy at room temperature is determined as ~ 21 mJ/m^2 [31, 32], which is consistent with the result obtained by X-ray diffraction measurements (i.e., 18.3–27.3 mJ/m^2) [33]. As the temperature decreases to 77 K, the SFE of the alloy is significantly reduced to 8 mJ/m^2 [31], leading to the formation of profuse fine twins and the improved tensile strength and ductility.

On the other hand, for the plastically deformed alloys the activation of slip and twinning depends on the initial orientations of the constituent crystals. The mechanical behaviors of the multi-principal-element alloy single crystals with different orientations have been reported in recent years [34–37]. For the Cantor alloy tensile deformed at 77 K, it is found that deformation twinning was activated in the crystals initially oriented with < 111 > and < 122 >, while no twining is found in the < 149 > and < 123 > single crystals [34]. When the initial orientation is [5$\bar{9}$1], dislocation slip, instead of deformation twinning, acts as the main mechanism at both 293 and 77 K [35]. The study on the CoCrNi alloy also shows that deformation twins tend to be activated in the [110], [111], and [123] single crystals under uniaxial tension at room temperature [36]. Moreover, the CoCrNi alloy shows the higher ductility compared with the 316 stainless steel and Hadfield steel, which is attributed to the extensive secondary twining and twin networks formed in the medium-entropy alloy at the late stage of deformation. Since the mechanical twins in the CoCrNi alloy are thinner than that in the conventional steels, more barriers to the interaction between dislocations are provided. This results in the higher capacity of dislocation storage and thus postpones the occurrence of necking. The consistent orientation-dependent mechanical behaviors have also been found in the Fe$_{40}$Mn$_{40}$Co$_{10}$Cr$_{10}$ alloy under uniaxial tension at room temperature [37].

As the above statements, the fcc HEA single crystals show different mechanical properties and deformation mechanisms with the varying initial orientations. However, due to the fact that the nanoscale characterization relying on in situ electron microscopy is complicated and difficult, the orientation-dependent mechanical behaviors of the HEAs at the atomic scale remain unclear. On the other hand, as the most favorable tool for in situ analysis of the microstructural evolution and deformation mechanism of materials during deformation, the molecular dynamics (MD) simulation has been widely used [18, 27, 38–41]. The activation of deformation twins has been predicted in the Cantor alloy under uniaxial tension at 0 K by simulations [27]. Moreover, compared with Fe$_{50}$Ni$_{50}$, Co$_{50}$Ni$_{50}$, and Ni, the larger lattice distortion in the Cantor alloy tends to promote dislocation nucleation. According to the MD simulations of the CoCrNi alloy, due to the local chemical ordering, the increased energy barrier to dislocation slip leads to the more significant lattice friction, thereby strengthening the alloy [38]. Besides, the simulations for the Co$_{25}$Ni$_{25}$Fe$_{25}$Al$_{7.5}$Cu$_{17.5}$ alloy have shown that the deformation-induced transformation from fcc to bcc phases follows the N-W orientation relationship [39]. However, the orientation-dependent mechanical properties of the fcc HEA single crystals and the underlying micromechanisms have not been investigated by atomistic simulations.

In this work, the uniaxial tensile behaviors of the Cantor alloy single crystals with various initial orientations at 300 K were studied systematically with the MD simulations. The micromechanical behaviors of the HEA single crystals are then compared with that of the low-entropy metallic materials (Cu and Fe$_{50}$Ni$_{50}$). Based on the in situ analysis of the deformed materials at the atomic scale, the following questions will be answered: (1) how the mechanical property and micromechanism of the fcc-structured HEA under uniaxial tensile deformation depend on initial orientation? (2) whether the orientation-dependent mechanical behavior in the HEA is consistent with that in conventional materials? and (3) what is the origin of the different micromechanical behaviors between high-entropy and low-entropy materials? The results reveal the orientation-dependent deformation mechanisms of the fcc materials at the atomic scale and thus provide theoretical guidance for the design of high-performance HEAs.

2 Methods and Models

Uniaxial tensile deformation of the FeMnCoCrNi HEA single crystals with different orientations at 300 K is simulated. The size of the MD model is 10 (X) nm × 10 (Y) nm × 20 (Z) nm with approximately 180,000 atoms. The orientation of the single crystals is defined as (hkl)[uvw], where [hkl] is parallel to the normal direction (ND) of the rolled plane and [uvw] is parallel to the rolling direction (RD). The selected initial orientations, i.e., (100)[001], (001)[110], (11$\bar{2}$)[111], and (11$\bar{1}$)[112], are typically found in the recrystallized or the rolled fcc materials. The (1$\bar{5}$3)[123] orientation is also

Table 1 Initial orientations of the different single crystals

Orientation	X	Y	Z
Cube	[100]	[010]	[001]
Rotated-cube	[001]	[1$\bar{1}$0]	[110]
Copper	[11$\bar{2}$]	[$\bar{1}$10]	[111]
Brass-R	[11$\bar{1}$]	[$\bar{1}$10]	[112]
\	[1$\bar{5}$3]	[30$\bar{1}$]	[123]

The tension direction is parallel to the Z axis

selected because it is located inside the stereographic triangle and may show different mechanical behaviors compared with other single crystals. The initial orientation of each single crystal is given in Table 1. In what follows, the uniaxial tensile direction, i.e., [uvw], is used to represent the orientation of the crystals. The tensile direction (Z) which is parallel to the RD is set as the periodic boundary condition. The other two orthogonal directions, i.e., X (//ND) and Y (//TD), are set as free boundary conditions. To obtain the evolution of different deformation systems and their influence on the mechanical properties under tensile loading, the maximum engineering strain (ε) of 0.5 is applied. Each single crystal is firstly relaxed at 300 K for sufficient time so that the pressure in the Z direction is zero, and then the uniaxial tension is applied on the model. The strain rate is 10^8/s and the time step is 5 fs, respectively. It should be mentioned that the single crystal simulations with an applied strain rate of 10^7/s have also been conducted and the results (mechanical responses and deformation mechanisms) are consistent with that using the strain rate of 10^8/s. The MD simulations are implemented with the open-source LAMMPS software [42]. The evolution of the atomistic structure is visualized using the OVITO software [43]. The different atomic structures and dislocation types are differentiated using the common neighbor analysis (CNA) [44] and the dislocation analysis (DXA) [45] algorithms, respectively. In order to quantitatively reveal the activation of various deformation systems under tensile loading, twin boundary, stacking fault and martensite with the hexagonal close-packed (hcp) structure are defined as one single layer, two layers and three or more layers of continuous hcp atoms, respectively.

To reveal the effect of lattice distortion on the orientation-dependent mechanical behaviors of the HEA, the deformation of two low-entropy materials, i.e., the binary Fe$_{50}$Ni$_{50}$ alloy and pure Cu, is also simulated. Previous experimental studies have shown that the SFEs of FeMnCoCrNi, Fe$_{50}$Ni$_{50}$, and Cu at 293 K are approximately 25, 79 and 45 mJ/m^2, respectively [46–48], and dislocation slip acts as the dominant deformation mechanism in all these materials at room temperature [27, 49, 50], which is the rational for comparing their mechanical behaviors. Here, the interactions of atoms

in FeMnCoCrNi, Fe$_{50}$Ni$_{50}$, and Cu are described with the modified embedded-atom method (MEAM) potential [27, 51]. Based on the MEAM potential used in this work, the lattice parameters of FeMnCoCrNi, FeNi and Cu at the ground state are calculated as 3.595, 3.583 and 3.615 Å, respectively, which are close to the data obtained by experiments and other theoretical predictions [6, 47, 48]. Moreover, the SFEs of the three materials are calculated to be −45, 19.3 and 42.5 mJ/m^2 at the ground state, respectively. The values of the HEA and pure Cu are consistent with that obtained by previous MD and/or ab-initio calculations [41, 48, 52]. As shown in Fig. S1 a_1-c_1 in the Supplementary material, different types of atoms are randomly distributed in both FeMnCoCrNi and Fe$_{50}$Ni$_{50}$ alloys. Accordingly, the single-atom potential energy is also distributed randomly in the materials (Fig. S1 a_2-c_2). In addition, compared with Fe$_{50}$Ni$_{50}$ and pure Cu, the distribution of atomic potential energy in the HEA is the most inhomogeneous.

3 Results and Discussion

3.1 Mechanical Behaviors of the FeMnCoCrNi Single Crystals

Stress–strain curves of the different FeMnCoCrNi single crystals deformed at 300 K are shown in Fig. 1. At the initial stage of deformation, the stress of each single crystal increases linearly with the increase of strain and reaches the peak value, which is regarded as the elastic regime. The Young's modulus $E_{[hkl]}$ of the crystals varies between 83 and 147 GPa. The [111] and [100] crystals show the largest and the smallest $E_{[hkl]}$, respectively. The orientation dependence
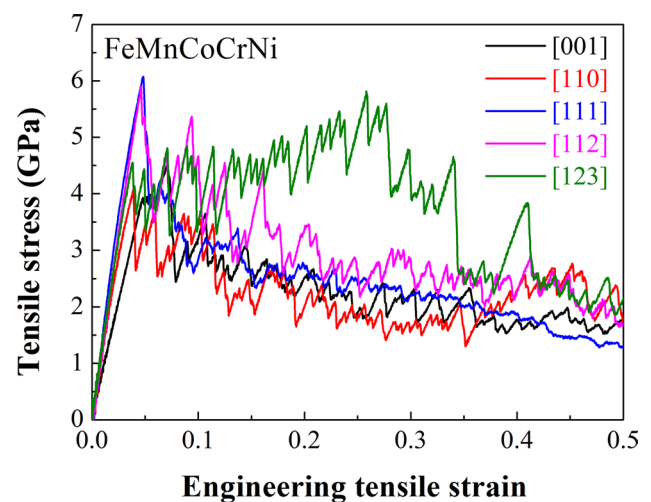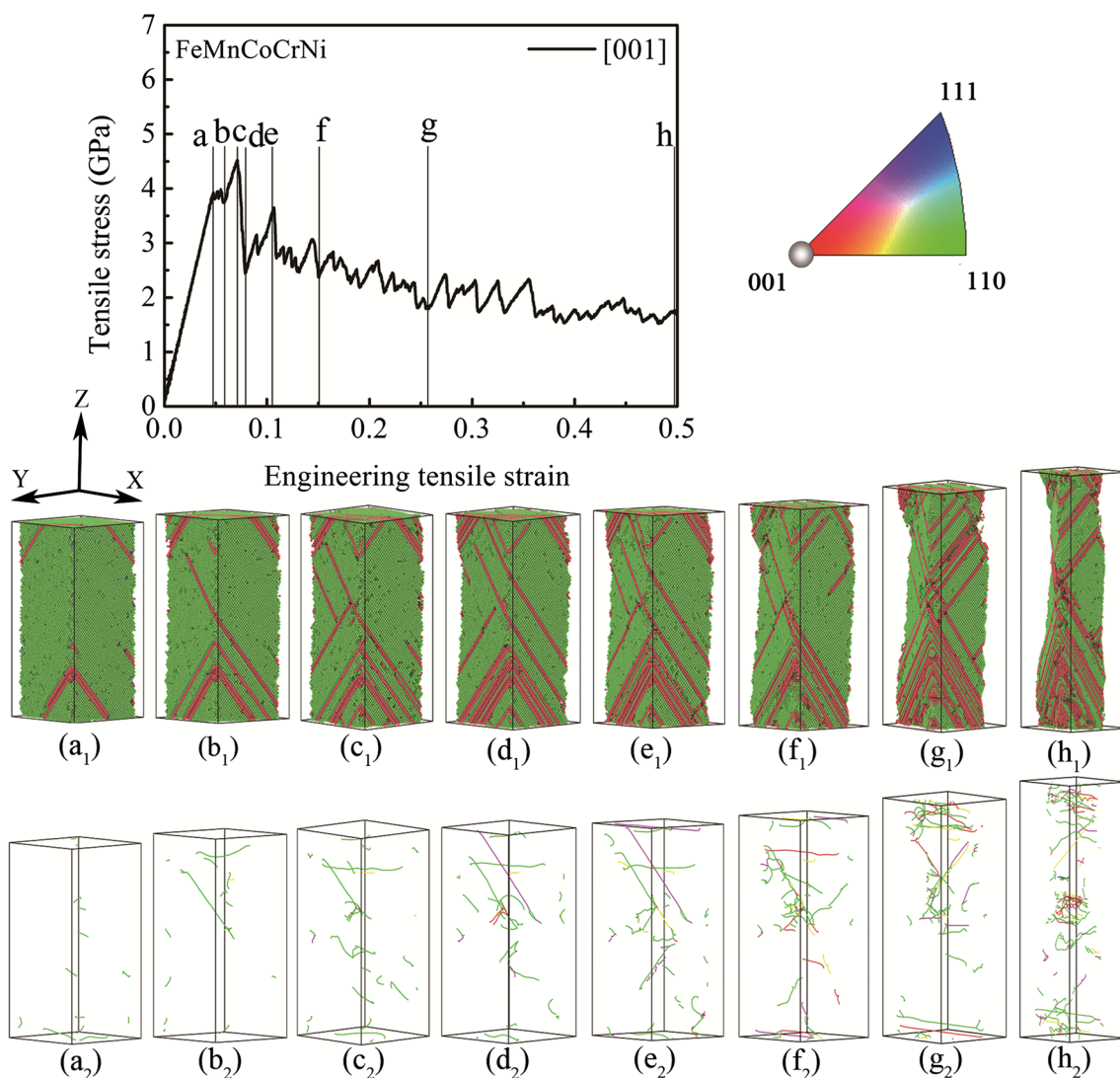

Fig. 1 Stress–strain curves of the FeMnCoCrNi single crystals with different initial orientations at 300 K and a strain rate of 10^8/s under uniaxial tension

of the Young's modulus is consistent with that found in the same alloy by Ab-initio calculations [53]. At the yield point, the engineering stress and strain of the models with different initial orientations are: 6.07 GPa and 0.0484 for the [111] crystal, 5.91 GPa and 0.0462 for the [112] crystal, 4.55 GPa and 0.038 for the [123] crystal, 4.09 GPa and 0.039 for the [110] crystal and 3.93 GPa and 0.0478 for the [001] crystal, respectively. Taking the [001] crystal as an example, when the material enters the plastic regime ($\varepsilon \geq 0.0478$), a small platform with fluctuation appears in the stress–strain curve, which is attributed to the nucleation and slip of Shockley partials. At a strain of 0.071, the stress reaches the maximum (4.52 GPa). Subsequently, the stress decreases rapidly with the increasing strain due to the activation of multiple

deformation mechanisms. Besides, during plastic deformation the stress–strain curves of all the studied crystals exhibit a serrated shape. With increasing deformation, the stress in each single crystal decreases except for the [123]-oriented material.

The microstructure and dislocation evolutions of the various single crystals during deformation are shown in Figs 2, 3, 4, 5, and 6. Figure 2 shows the simulation results of the [001] single crystal. When the strain is between 0.0478 and 0.071 (corresponding to the loading stage from point 'a' to 'c' in the stress–strain curve), nucleation and slip of Shockley partials have occurred, and dislocations are first generated at the free surfaces. As strain increases, dislocations slip through the whole crystal and escape from other

Fig. 2 Stress–strain curve of the FeMnCoCrNi single crystal with the [001] orientation. The inverse pole figure shows the initial orientation of the crystal. 'a'–'h' are some key points at different deformation stages. $\mathbf{a_1}$–$\mathbf{h_1}$ are microstructures corresponding to 'a'–'h.' In (a_1)-(h_1), ● and ● represent fcc and hcp structures, respectively. $\mathbf{a_2}$–$\mathbf{h_2}$ are dislocation line distributions corresponding to 'a'–'h.' In (a_2)-(h_2), ■ perfect, ■ Shockley, ■ stair-rod, ■ Hirth, ■ Frack, and ■ other
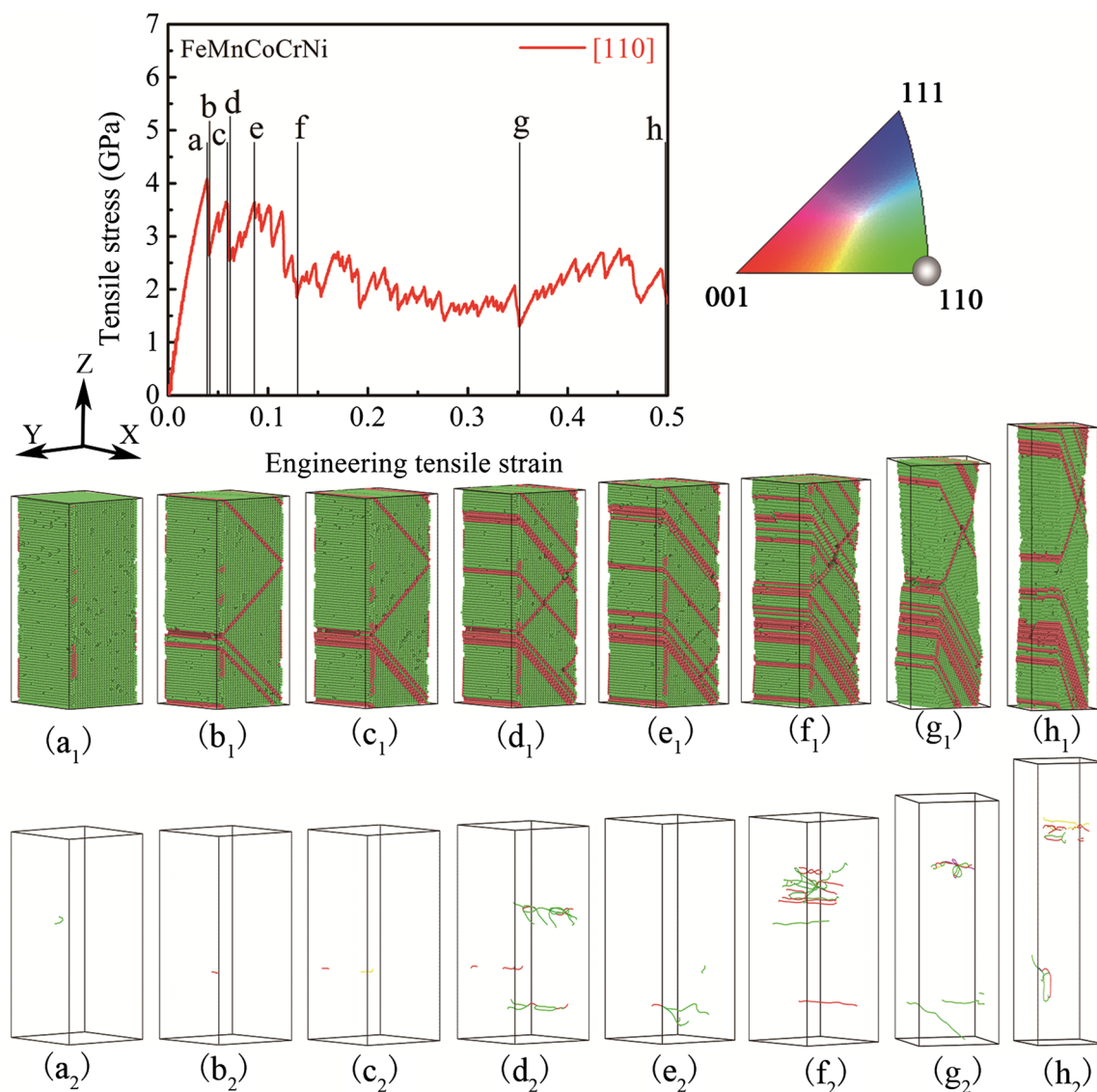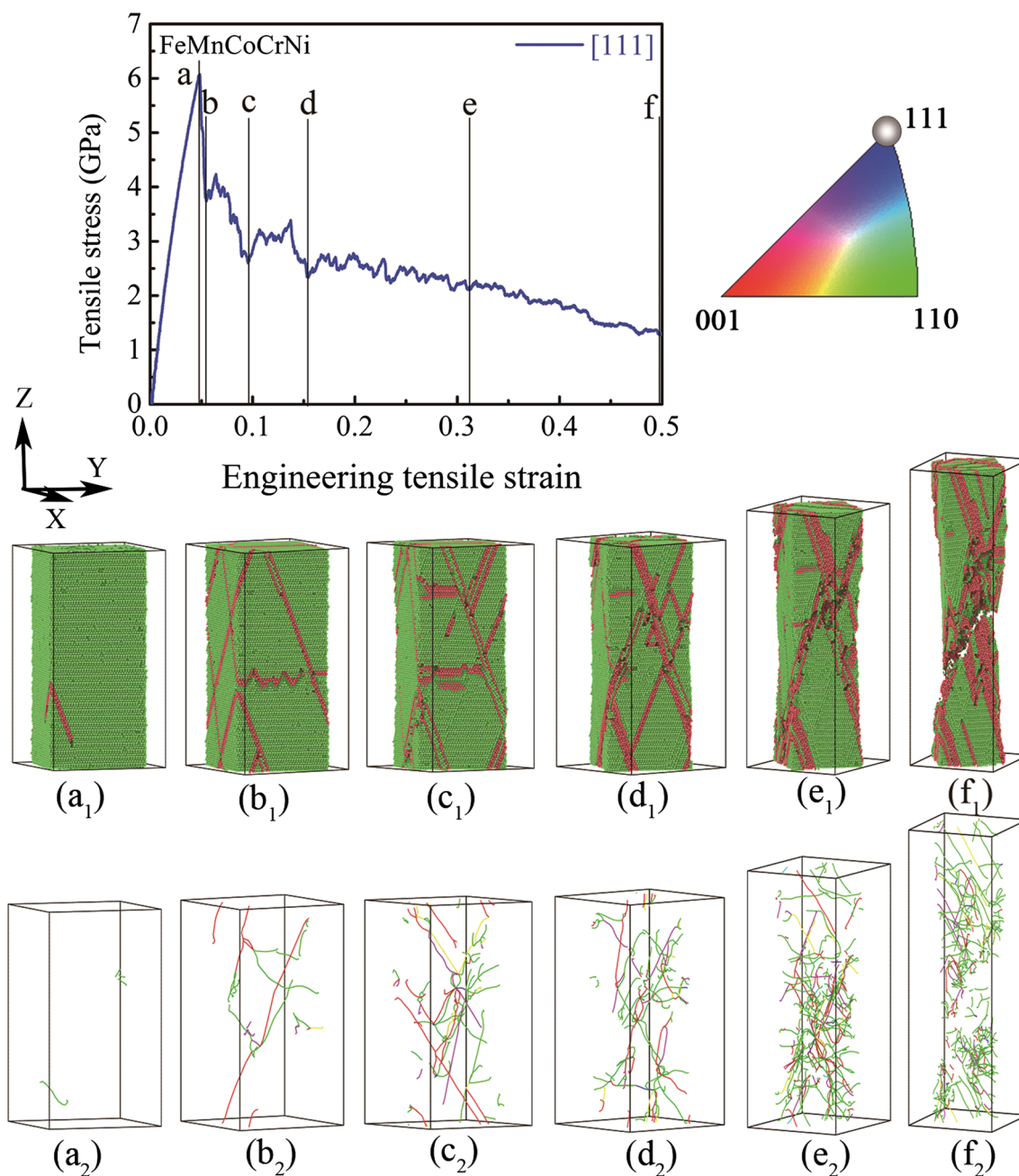
Fig. 3 Stress–strain curve of the FeMnCoCrNi single crystal with the [110] orientation. The inverse pole figure shows the initial orientation of the crystal. 'a'-'h' are some key points at different deformation stages. a_1–h_1 are microstructures corresponding to 'a'-'h.' a_2–h_2 are dislocation line distributions corresponding to 'a'-'h'

free surfaces. Intrinsic stacking faults are formed after dislocation slip (Fig. 2a1–c1). The dislocation distribution corresponding to this deformation stage is shown in Fig. 2a2–c2. The dislocations inside the single crystal are Shockley partials. As the strain increases (from point 'd' to 'h'), more dislocations are activated accompanied with the increased stacking faults. Meanwhile, other types of dislocations appear inside the crystal. With increasing strain, more stacking faults or dislocations in different directions interest and entangle with each other, as shown in Fig. 2d1–h1 and d2-h2. When strain is elevated further (from point 'g' to 'h'), necking starts to occur in the area where stacking faults and dislocations are entangled. A small amount of hcp-martensite lamellas are formed near the necked region,

and the dislocation density in this region is relatively high (Fig. 2g1–h1 and g2–h2).

Figure 3 shows the evolution of the microstructure and dislocations of the [110]-oriented crystal during deformation. The yield point is reached at a strain of 0.039 (corresponding to the point 'a' in the stress–strain curve), and Shockley partials are nucleated on the free surfaces of the model (Fig. 3a1 and a2). As strain increases, the stress rapidly drops to the point 'b,' and the Shockley partials slip through the entire crystal and escape from other free surfaces. Intrinsic stacking faults that run through the entire single crystal are then left (Fig. 3b1), and no dislocation lines are found (Fig. 3b2). With increasing deformation, multiple Shockley partials, stacking faults, twins, and

Fig. 4 Stress–strain curve of the FeMnCoCrNi single crystal with the [111] orientation. The inverse pole figure shows the initial orientation of the crystal. 'a'-'f' are some key points at different deformation stages. a_1–f_1 are microstructures corresponding to 'a'-'f.' a_2–f_2 are dislocation line distributions corresponding to 'a'-'f'

hcp-martensite are triggered successively within the crystal, leading to the fluctuating tensile stress with increasing strain (from point 'c' to 'h'). At this deformation stage, stacking faults in different directions are formed, as shown in Fig. 3d1. Meanwhile, the dislocation lines at the intersection of the stacking faults also intersect and entangle with each other (Fig. 3d2). When the strain increases to the point 'f,' twin boundaries that are identified as single-layered hcp atoms are formed, as seen in Fig. 3f1. With

further straining, the number of the twin boundaries continuously increases (Fig. 3f1–h1), and the hcp-martensite laths also appear within the crystal (Fig. 3c1–h1). It is worth noting that during deformation, the [110]-oriented crystal is always uniformly elongated without apparent necking, suggesting that this material has a good ability of uniform deformation. In addition, the dislocation density in this crystal is low at various stages of deformation (Fig. 3a2–h2).
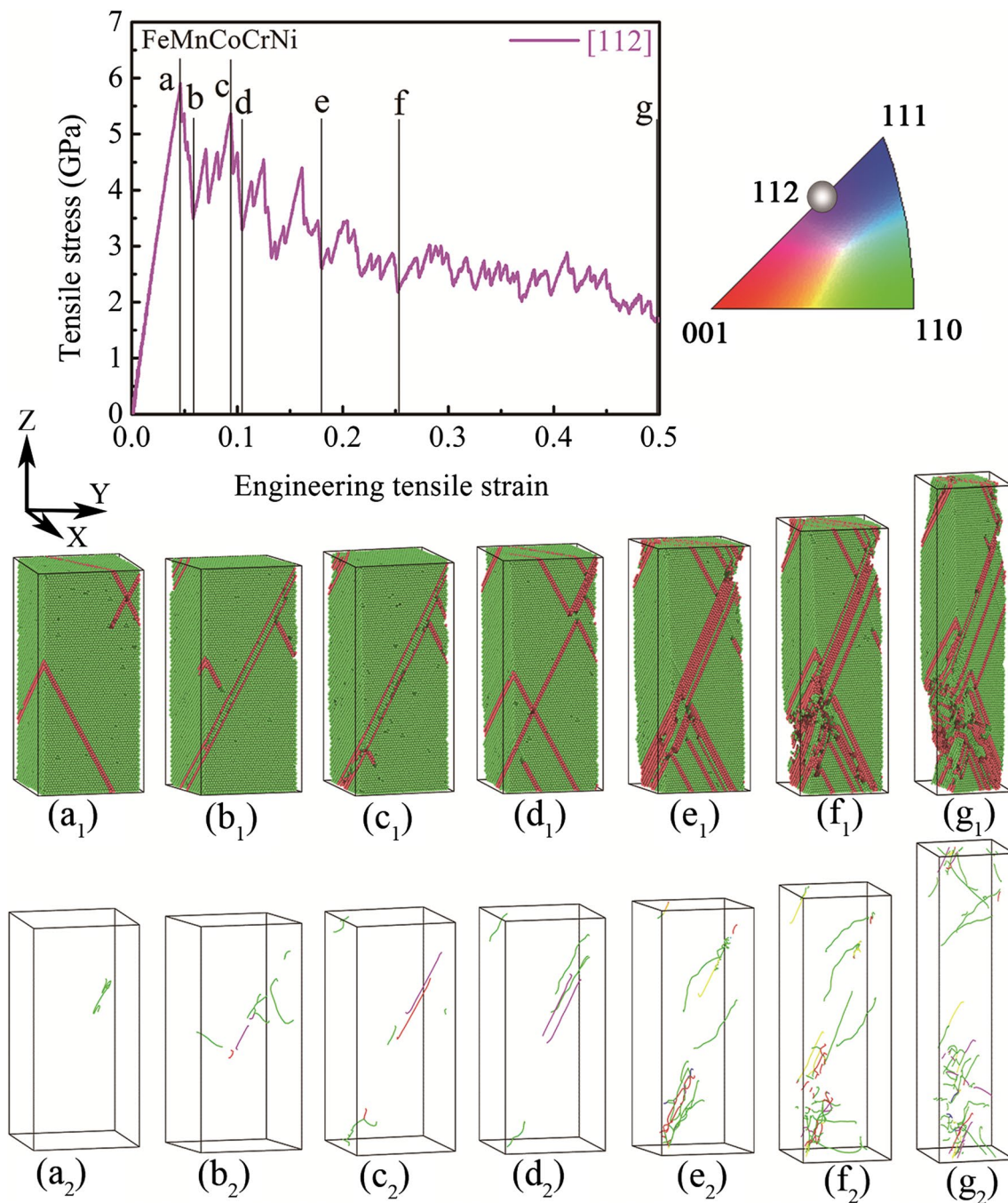
Fig. 5 Stress–strain curve of the FeMnCoCrNi single crystal with the [112] orientation. The inverse pole figure shows the initial orientation of the crystal. 'a'-'g' are some key points at different deformation stages. a_1–g_1 are microstructures corresponding to 'a'-'g.' a_2–g_2 are dislocation line distributions corresponding to 'a'-'g'

For the [111]-oriented single crystal, when the strain is 0.0484, the yield point 'a' in the stress–strain curve is reached (Fig. 4), and the Shockley partials nucleation appears on the free surfaces (Fig. 4a1). When the strain increases to point 'b,' stacking faults and dislocations in different directions are formed (Fig. 4b1 and b2). At this deformation stage, part of the stress within the crystal starts

to be released, and both stacking faults and dislocations intersect with each other during the subsequent deformation (Fig. 4b1–f1 and b2–f2). When the strain increases to point 'c,' deformation twins are formed (Fig. 4c1). When the strain further increases to the point 'e,' the hcp-martensite laths in the form of multilayered hcp atoms can be identified (Fig. 4e1). During the whole period of deformation,
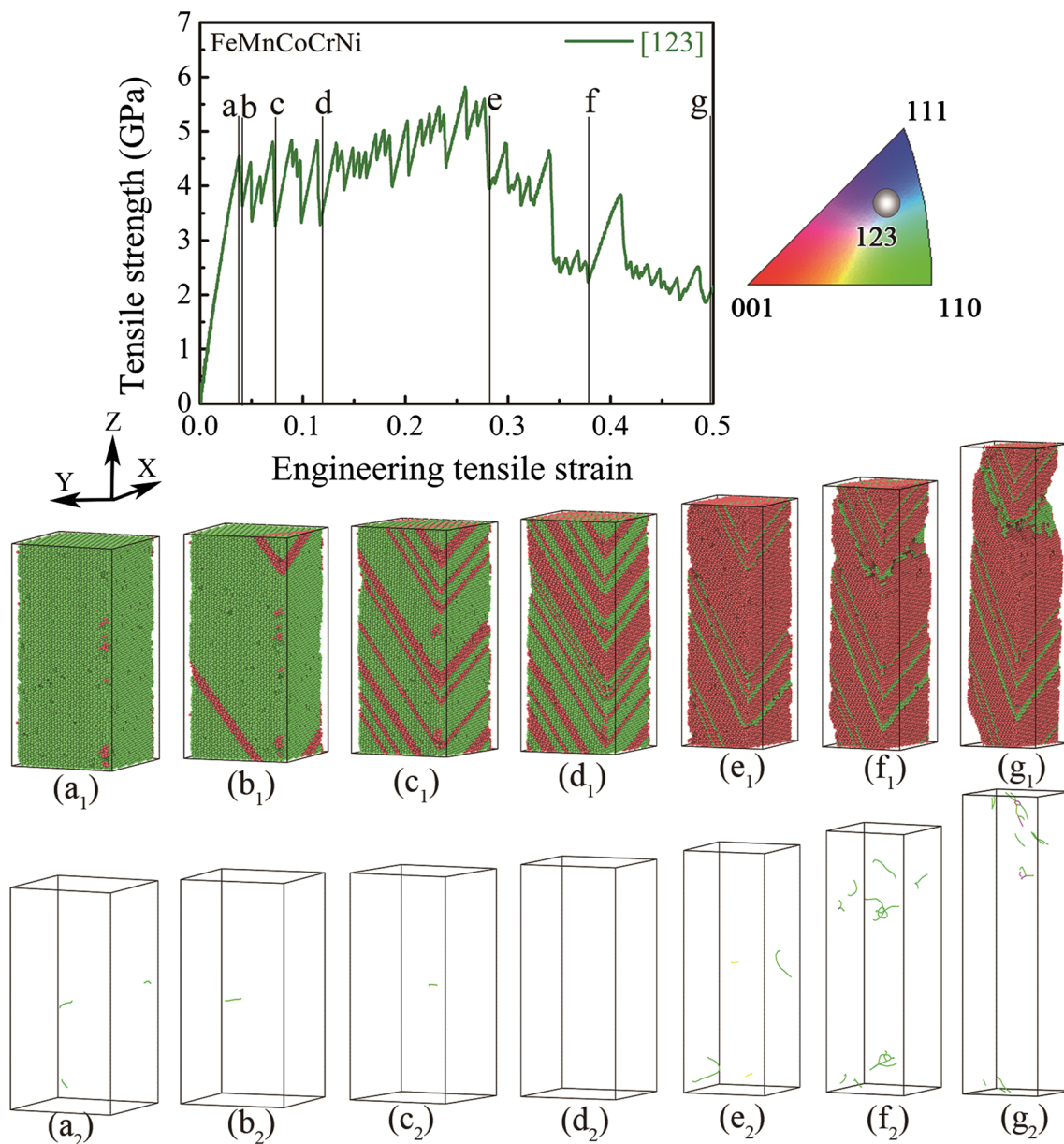
Fig. 6 Stress–strain curve of the FeMnCoCrNi single crystal with the [123] orientation. The inverse pole figure shows the initial orientation of the crystal. 'a'-'g' are some key points at different deformation stages. **a₁–g₁** are microstructures corresponding to 'a'-'g.' **a₂–g₂** are dislocation line distributions corresponding to 'a'-'g'

the dislocation density inside the single crystal increases continuously with the increasing strain (Fig. 4a2–f2). At 0.5 strain, significant necking appears in the crystal (Fig. 4f1).

For the [112]-oriented single crystal, the sample yields at a strain of 0.0462 (corresponding to the point 'a' in the stress–strain curve in Fig. 5). At this loading stage, slip of Shockley partials occurs (Fig. 5a2), leading to the formation of intrinsic stacking faults (Fig. 5a1). As the strain increases from point 'b' to 'c,' deformation twins are formed (Fig. 5b1–c1). When the strain continues to increase to point 'd,' those twins disappear and stacking faults evolve again,

as shown in Fig. 5d1. When the strain further increases to point 'e,' the hcp-martensite lamellas are formed (Fig. 5e1). In addition, necking occurs at this loading point. As the strain further increases, the dislocation density continues to increase (Fig. 5f2–g2), and a high density of dislocations are identified at the necked region.

Figure 6 shows the simulation results of the [123] single crystal. The crystal starts to yield at a strain of 0.038 (corresponding to the point 'a' in the stress–strain curve). At this time, Shockley partials are nucleated on the free surfaces of the model (Fig. 6a1 and a2). As the strain increases to point

'b,' Shockley partials slip across the entire crystal, leading to the formation of intrinsic stacking faults (Fig. 6b1) and the released stress. When the strain increases to point 'c,' stacking faults continue to increase, and either stacking faults intersection or dislocation entanglement is not found in the crystal (Fig. 6c1 and c2). When the strain reaches point 'd,' deformation twins are formed, as seen in Fig. 6d1. It should be noted that in the deformation stage from point 'c' to 'g,' multiple stacking faults are superimposed to form the hcp-martensite, and the martensitic lamellae are thickened continuously with deformation. Besides, necking occurs in the crystal at around 0.5 strain and only a few dislocations are identified at various deformation stages (Fig. 6a2–g2). The Schmid factors of Shockley partials in the single crystals with various initial orientations are shown in Table S1. The maximum Schmid factors are found corresponding to the different slip systems for each single crystal under uniaxial tensile loading, except for the [123]-oriented crystal. Therefore, as the deformation proceeds, both stacking faults and dislocations in different directions are activated, whereas in the [123] crystal only the stacking faults or dislocations in one direction are activated. It is also found that the activation of the deformation systems in the present FeMnCoCrNi single crystals follows the Schmid law.

3.2 Discussion

3.2.1 Orientation Dependence of Micromechanical Behavior in the FeMnCoCrNi HEA

The densities of total dislocation lines and different types of dislocations as a function of the tensile strain in the various FeMnCoCrNi single crystals are shown in Fig. 7. With increasing loading, dislocation density increases in all crystals, and Shockley partials contribute the most to the total dislocation density among the different types of dislocations. The [001], [111], and [112] orientations show the higher total dislocation densities than others. Moreover, compared with the [110] and [123] crystals, the above-mentioned three orientations show the more significant necking at around 0.5 strain (Figs. 2, 4, and 5). We also note that in the plastic regime the stress of the [001], [111], and [112] crystals continuously decrease with deformation, indicating that the high dislocation densities are not sufficient for strengthening the materials. Namely, necking tends to occur in those single crystals. In addition, more stacking faults are formed in the three crystals, due to that stacking faults are resultant from the slip of Shockley partials. For the [110] crystal under deformation, the lower dislocation density compared with other samples is attributed to the activation of twinning and martensitic transformation in the former. The massive formation of the hcp-martensite in the [123] crystal leads
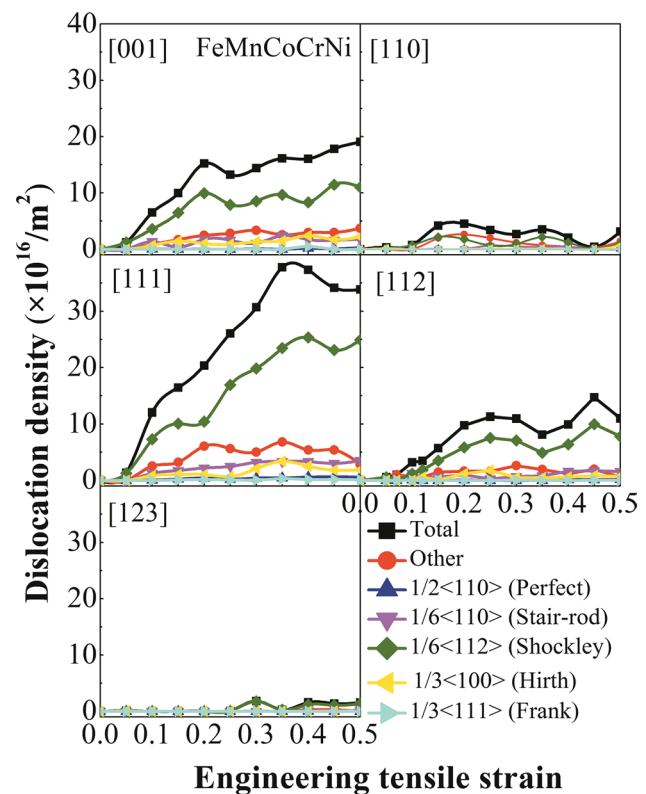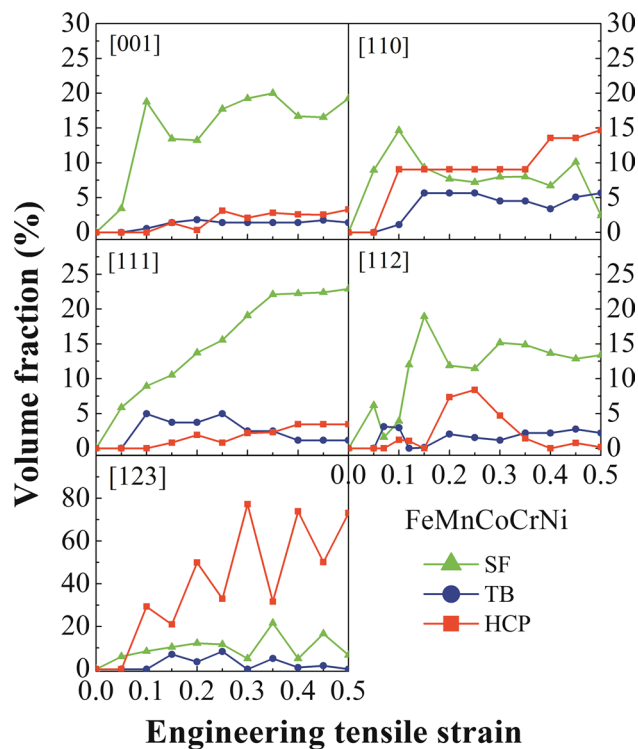

Fig. 7 Evolution of dislocation density in the FeMnCoCrNi single crystals with different initial orientations

to the smallest dislocation density among the studied single crystals.

Evolution of atomic volume fractions in the fcc, hcp and unknown structures for the HEA is shown in Fig. S2. As the hcp structure includes atoms in stacking faults, twin boundaries and hcp-martensite, the volume fraction of the hcp structure (V_{hcp}) is used to represent the fraction of the plastic deformation systems. Fractions of the fcc and the unknown structures are represented as V_{fcc} and $V_{unknown}$, respectively. Throughout the tensile deformation, the fcc-type atoms generally decrease with the increasing deformation in the various single crystals, accompanied by the increase of the hcp and the unknown-type atoms. The evolution of different types of atoms in the [001]- and [110]-oriented crystals is more stable compared with that of other crystals. The main deformation mechanism in the [001] crystal is stacking faults, while in the [110] crystal more hcp-martensite and deformation twins are formed in addition to stacking faults. The [123] crystal shows the largest increase of the hcp type atoms among the studied orientations, which is due to its significant hcp-martensitic transformation. Besides, the unknown-type atoms in the [111] and [112] single crystals show the more significant increase with deformation. This is because apparent necking occurs in these samples in the

late stage of deformation and the necked area is partially amorphous.

In order to quantitatively reveal the activation of various deformation systems in the FeMnCoCrNi single crystal under tensile loading, volume fractions of stacking faults (V_S), twins (V_T) and hcp-martensite (V_M) as a function of engineering strain are given in Fig. 8. Among the studied orientations, the [001], [111], and [112] crystals show the larger V_S in the plastic regime, suggesting that stacking fault is the dominant mechanism. In the [123] crystal, the hcp-martensite transformation is the dominant deformation mode, as the significant increase of V_M is identified when the strain reaches ~ 0.05. In this crystal, only the stacking faults or dislocations in one direction are activated; thus, intersection and entanglement of different stacking faults are not identified. This is conducive to the formation of stacking faults and promotes the martensitic transformation. One may also note that at above 0.25 engineering strains, the volume fraction of hcp-martensite in the [123] HEA crystal fluctuates severely with deformation. This is related to the fluctuating evolutions of stacking faults as well as atomic volume fractions of the fcc and hcp atoms (Fig. S2). This may be ascribed to the reverse transformation of martensite in the HEA [25]. However, this is beyond the scope of the current paper. The V_S, V_T, and V_M are similar in the [110] crystal, and the development of V_T is more significant than that in other crystals. This indicates that twinning is another important deformation mode in addition to stacking faults and martensitic transformation. Therefore, twinning tends to be activated in the most single crystals except for that initially oriented with [001]. This is consistent with the orientation-dependent twinning in $Fe_{40}Mn_{40}Co_{10}Cr_{10}$, FeMnCoCrNi, and CoCrNi HEAs as observed by experiments [34, 36, 37].

3.2.2 Comparison of Micromechanical Behaviors between HEA and Low-entropy Materials

Three crystals, i.e., the [001]-, [110]-, and [123]-oriented single crystals, are selected to reveal the difference of micromechanical behavior between high-entropy and low-entropy materials. Stacking faults, twinning and martensitic transformation are the dominant deformation modes in those HEA single crystals, respectively. The stress–strain curves of the differently oriented FeMnCoCrNi, $Fe_{50}Ni_{50}$, and Cu single crystals are shown in Fig. 9. For the [001] orientation, the stress of FeMnCoCrNi is lower than the low-entropy materials in the deformation stages of $0 < \varepsilon < 0.1$ and $0.3 < \varepsilon < 0.5$ (Fig. 9a). For the [110] orientation, the HEA also shows the lower stress than that of $Fe_{50}Ni_{50}$ and Cu. However, when 0.35 strain is reached both the HEA and the $Fe_{50}Ni_{50}$ alloy show the higher stress than Cu (Fig. 9b). For the [123] orientation, the stress in the HEA is still lower than the low-entropy materials in the transition stage from elastic to plastic. It should be emphasized that the predicted stress corresponding to the elastic–plastic transition point does not represent the critical resolved shear stress that is commonly discussed in experimental work. The yield point predicted by MD simulations denotes the deformation stage at which Shockley partials nucleate in one perfect single crystal in the nanoscale. During the subsequent deformation, the HEA exhibits the higher flow stress than Cu (Fig. 9c), which is consistent with that oriented with [110]. These results show that as the types of element decrease, i.e., corresponding to the lowered configurational entropy, the critical stress required for the elastic-to-plastic transition increases [27]. This makes dislocations nucleate more readily in the high-entropy solid solution, so that the HEA undergoes plastic deformation at a lower stress level. Secondly, for each studied material under uniaxial tension, the [110] crystal shows the smallest yield stress. This indicates that dislocations in this crystal are easier to nucleate compared with that oriented with [001] and [123], which is also consistent with the orientation-dependent dislocation behaviors in pure copper as predicted by MD simulations [54, 55].

Figure 10 shows the microstructures and dislocation distributions in the FeMnCoCrNi, $Fe_{50}Ni_{50}$, and Cu single crystals at a strain of 0.5. For the [001] orientation, more
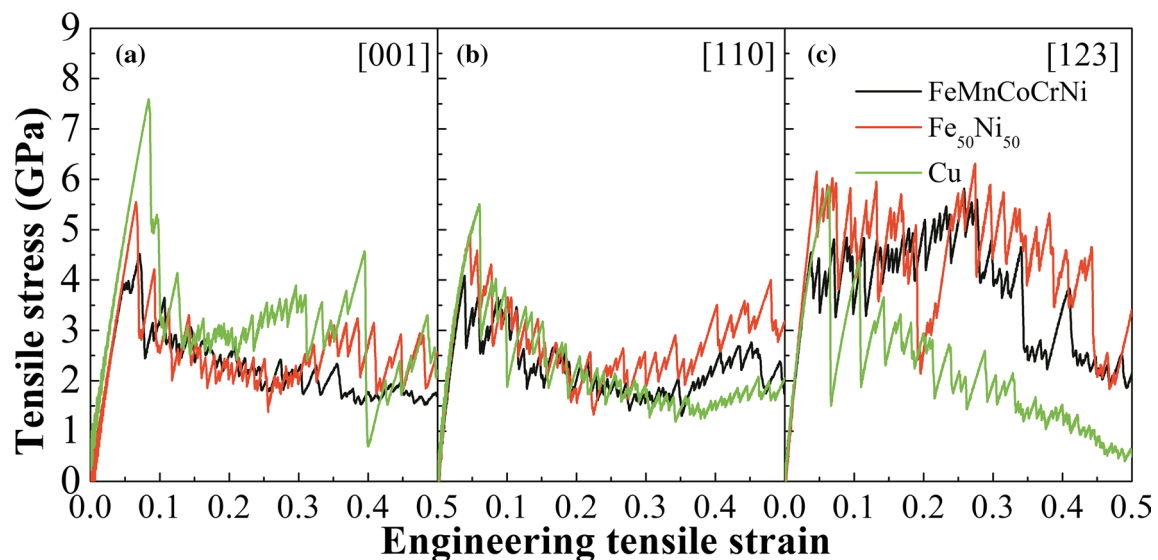

Fig. 8 Volume fraction evolution of stacking faults, twin boundaries and hcp-martensite in the FeMnCoCrNi single crystals with different initial orientations. SF stacking fault; TWB twining boundary; HCP hcp-martensite

Fig. 9 Stress–strain curves of FeMnCoCrNi, $Fe_{50}Ni_{50}$, and Cu single crystals with different initial orientations

stacking faults and hcp-martensite are formed in the HEA single crystal compared with $Fe_{50}Ni_{50}$ and Cu. Necking occurs in the HEA, and significant dislocation entanglement is then identified in the necked area (Fig. 10a). For the $Fe_{50}Ni_{50}$ and Cu single crystals with the same orientation, deformation is relatively uniform (Fig. 10d and g). At this time, the stress level of the HEA is lower than that of $Fe_{50}Ni_{50}$ and Cu. This is attributed to the significant non-uniform deformation of the former material, i.e., the localized strain at the necked position.

It is worth noting that at this deformation stage, only a small amount of stacking faults are activated in the $Fe_{50}Ni_{50}$ crystal oriented with [001] and dislocation slip is not obvious. By tracing the deformation process, this is attributed to the migration of twin boundaries in the material. As shown in Fig. S3, when the strain is between 0.15 and 0.2, a twin boundary on the top of the model gradually migrates to the upper corner with deformation. Meanwhile, stacking faults and hcp-martensite do not evolve significantly. The migration of twin boundaries has also been observed in the [110]-oriented HEA crystal and the [001]-, [110]-, and [123]-oriented Cu crystals. This is consistent with the experimental characterization of the submicron-scale [001]- and [110]-oriented Cu micropillars under uniaxial compression tests [56]. The migration and sliding of twin boundaries are closely related to the Schmid factor. The behavior of a twin boundary can be predicted by α_M, i.e., $\alpha_M = SF_M^{LP}/SF_M^{TP}$, where SF_M^{LP} and SF_M^{TP} are the Schmid factors of the leading and the trailing partial dislocations, respectively. Twin boundary migration occurs when α_M is not equal to one. When $\alpha_M = 1$, twin boundary sliding would occur.

For the [110] orientation, both FeMnCoCrNi and $Fe_{50}Ni_{50}$ crystals are deformed uniformly at 0.5 strain, whereas the Cu single crystal shows the significant necking. Deformation twins have been activated in all three materials (Fig. 10b, e, h). However, more stacking faults are found in the $Fe_{50}Ni_{50}$ alloy compared with FeMnCoCrNi and Cu, and hcp-martensite lamellas are formed in FeMnCoCrNi and $Fe_{50}Ni_{50}$. Significant dislocation entanglement only appears in the HEA but not in the low-entropy single crystals.

For the [123] orientation, a large amount of hcp-martensite is formed in the FeMnCoCrNi single crystal after deformation, and only a small amount of fcc-type atomic layers are embedded between the hcp lamellas. Necking accompanied with a small amount of dislocations occurs in the upper of the model (Fig. 10c). The $Fe_{50}Ni_{50}$ crystal appears to be slightly necked, and deformation twins, stacking faults and hcp-martensite are uniformly distributed inside the model (Fig. 10f). In addition, dislocations are identified in the area where stacking faults, twin boundaries, and hcp-martensite lamellas intersect. For the Cu crystal, hcp-martensite and twins are also activated; however, obvious necking occurs in this sample. The cut plane of the necked position entangled with dislocations is parallel to the (111) plane and the twin boundary (Fig. 10i). Due to this inhomogeneous deformation, the stress level of Cu is lower than that of FeMnCoCrNi and $Fe_{50}Ni_{50}$.

To this stage, it is clear that for the FeMnCoCrNi alloy, necking accompanied with dislocation entanglements occurs in the both [001]- and [123]-oriented crystals, whereas the [110] crystal deforms more uniformly. In addition, dense stacking faults and a small amount of hcp-martensite are formed in the [001] crystal. The [110] crystal shows more

[001]   [110]   [123]
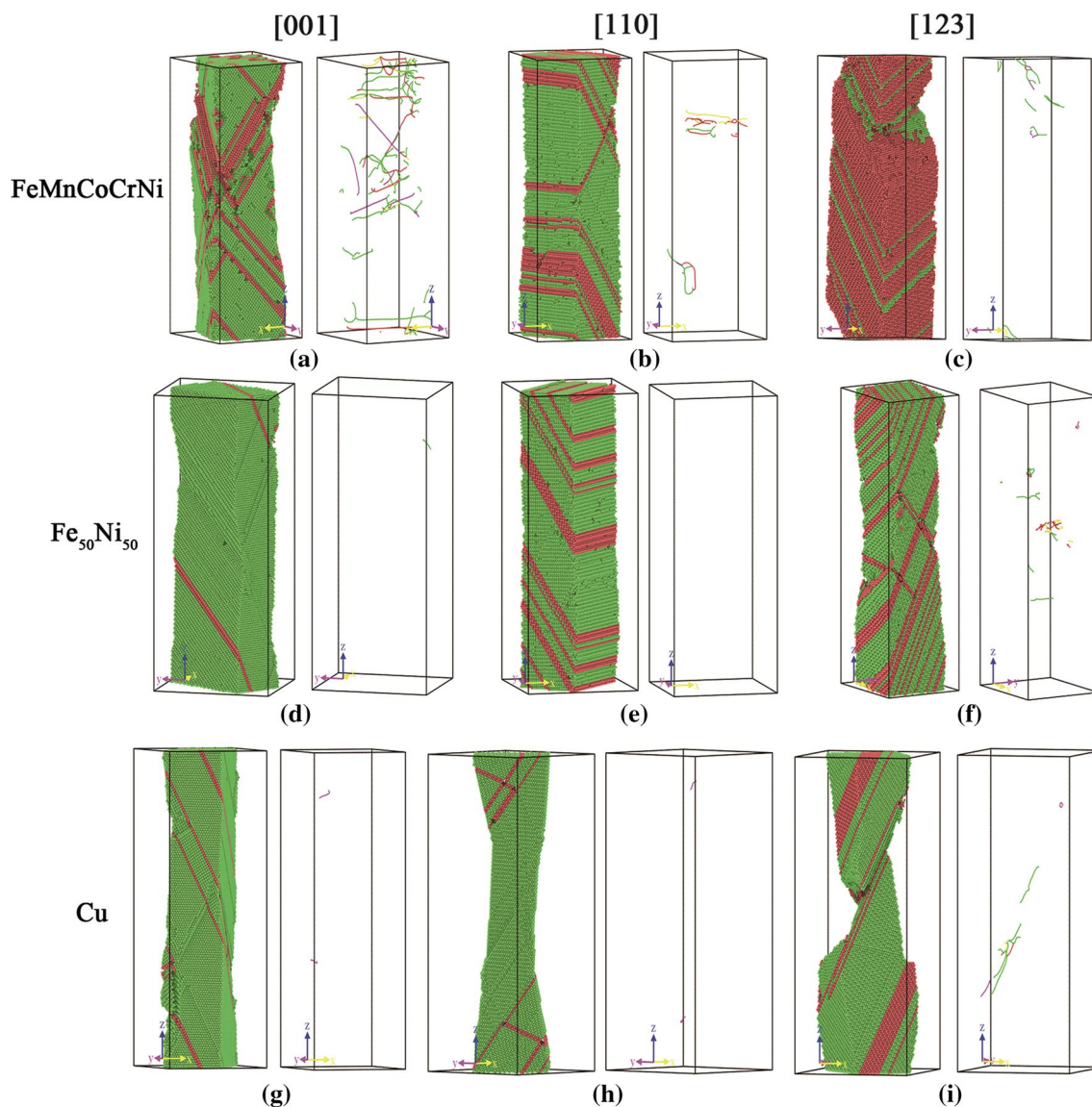
Fig. 10 Atomic structure and corresponding dislocation line distribution in FeMnCoCrNi, Fe$_{50}$Ni$_{50}$, and Cu single crystals with different initial orientations at a tensile strain of 0.5

significant twinning compared with the [001] and [123] crystals. In the [123] crystal, the hcp-martensitic transformation dominates deformation. For the Fe$_{50}$Ni$_{50}$ alloy, the [001] and [110] crystals deform uniformly, and the [123] crystal shows the slight necking. Compared with the [001]-oriented crystal, more twinning and martensitic transformation are activated in the [110] and [123] crystals. For Cu, the [001] crystal deforms uniformly, whereas the [110] and [123] crystals show the significant necking. Stacking faults and twinning are the dominant deformation modes in the [001] and [110] Cu crystals, while the martensitic transformation is the main mechanism in the crystal oriented with [123]. The evolution of dislocation density for the FeMnCoCrNi, Fe$_{50}$Ni$_{50}$ and Cu single crystals is shown in Fig. S4. For the

[001] and [110] orientations, the total dislocation densities in FeMnCoCrNi are higher than that in Fe$_{50}$Ni$_{50}$ and Cu. For the [123] orientation, the total dislocation density in either HEA or low-entropy materials is insignificant, and a slight increase of dislocations is only identified when the strain reaches 0.35. For the FeMnCoCrNi crystals, the total dislocation density from high to low is in the order of [001], [110], and [123].

3.2.3 Effect of Lattice Distortion on the Deformation Mechanisms

Due to the difference in the atomic radius of various elements, lattice distortion in FeMnCoCrNi, Fe50Ni50 and Cu

is different. Lattice distortion is quantitatively described as the difference in atomic size δ [15, 57], i.e.,

$$\delta = 100\sqrt{\sum_{i=1}^{n} c_i\left(1 - \frac{r_i}{\bar{r}}\right)^2},$$

where n is the type number of element, ci and r_i are the atomic percentages and the atomic radius of the element i, respectively. $\bar{r}$ is the average atomic radius. The δ values of FeMnCoCrNi, Fe50Ni50, and Cu are calculated to be 1.8, 1.19, and 0, respectively. Namely, the HEA shows the more significant lattice distortion than the low-entropy materials, which prevents dislocations from sliding out of the free surfaces of one sample. Accordingly, more dislocations are stored within the HEA and the dislocation storage capacity of the material is enhanced. Although dislocations are prone to nucleate on the free surfaces of a model under deformation, the lattice distortion in the HEAs may prevent dislocations from slipping out of the free surfaces. Therefore, a large number of dislocations intersect and entangle with each other, resulting in necking at some positions with dense dislocations (Fig. 10a).

To reveal deformation mechanisms of the materials with different configurational entropies, the atomic volume fraction evolutions of the fcc, hcp, and unknown structures in the FeMnCoCrNi, Fe50Ni50, and Cu single crystals with deformation are shown in Fig. S5. For the [001] orientation, compared with the Fe50Ni50 and Cu crystals the HEA shows a more significant increase of Vhcp with increasing tensile strain and the maximum fraction reaches ~25%. For the [110] orientation, Vhcp increases with deformation in all three materials, and the maximum fraction of the hcp phase is ~ 37% in $Fe_{50}Ni_{50}$. With the initial orientation of [123], Vhcp also increases significantly with deformation and reaches ~ 78% in the HEA at a tensile strain of 0.5. In comparison, the evolution of Vhcp in Fe50Ni50 and Cu crystals is moderate and does not exceed 40% at 0.5 strain. For the same material with different initial orientations, Vhcp in the [123]-oriented HEA shows the more significant increase than other orientations. For Fe50Ni50 and Cu, the evolutions of Vhcp in the crystals oriented with [110] and [123] are similar for each material and more hcp-martensite is formed compared with the [001] orientation.
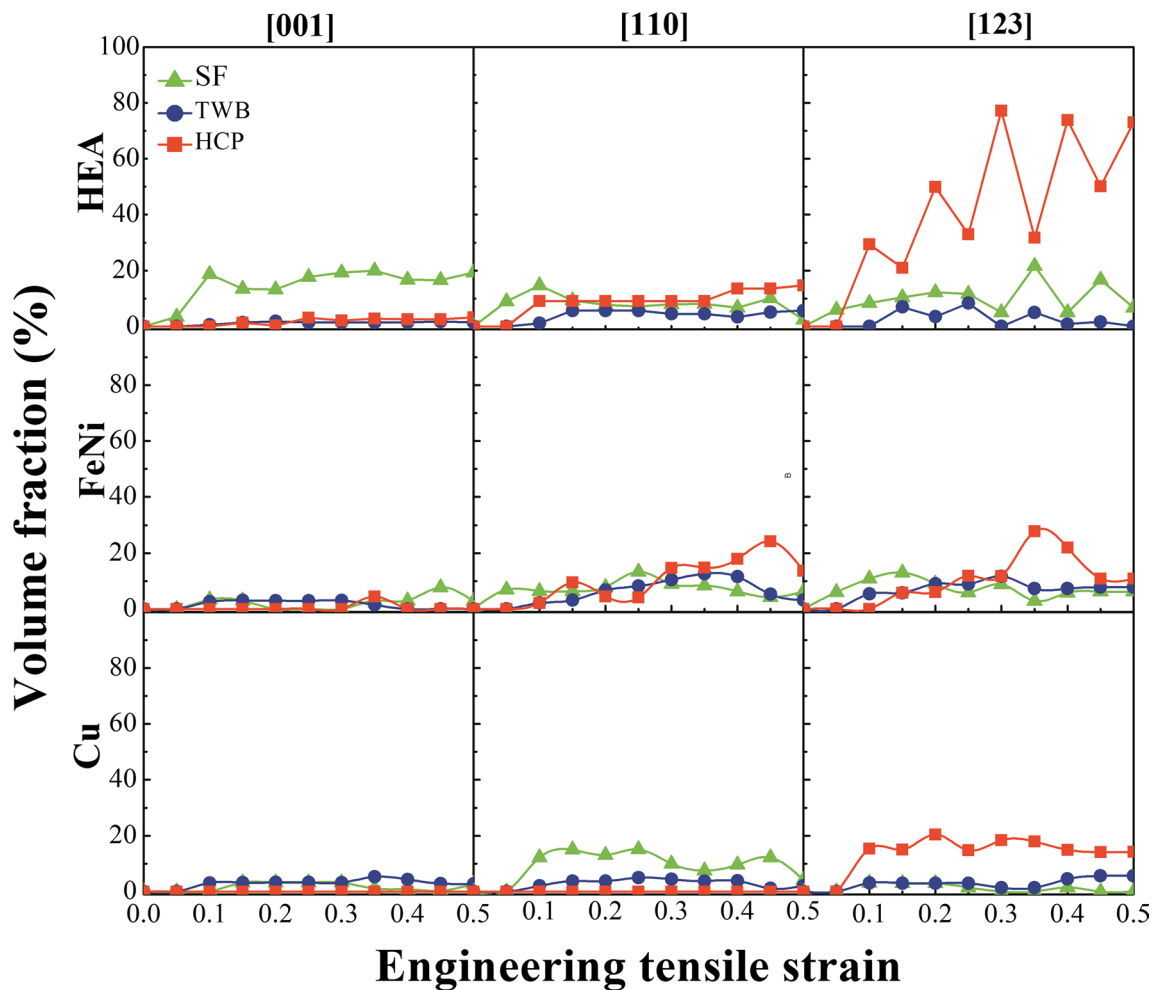
The volume fraction evolution of stacking faults, twin boundaries, and hcp-martensite in each single crystal is shown in Fig. 11. For the [001] orientation, the activation of stacking faults in the HEA is more significant than that in $Fe_{50}Ni_{50}$ and Cu. Meanwhile, more twins are formed in the low-entropy materials and all three materials show the minor hcp-martensite formation. During plastic deformation, the stress in both $Fe_{50}Ni_{50}$ ($0.25 < \varepsilon < 0.35$) and Cu ($0.2 < \varepsilon < 0.4$) single crystals shows an increasing tendency

when the tensile strain reaches ~ 0.2 (Fig. 9a). This corresponds to the larger volume fraction of twin boundaries in these materials, i.e., the more significant twinning that contributes to the higher work hardening and uniform plastic deformation of the samples. However, the stress in the [001]-oriented HEA continues to decrease with deformation. A higher dislocation density is found in this sample than the low-entropy ones (Fig. S4); however, this is not sufficient to provide good work hardening for the HEA.

For the [110] orientation, the volume fraction of stacking faults in the three materials is similar at various deformation stages. The HEA and $Fe_{50}Ni_{50}$ materials show more activation of twins and hcp-martensitic transformation compared with Cu. The migration of twin boundaries in Cu leads to the non-uniform deformation of the sample, which makes its stress level lower than that of $Fe_{50}Ni_{50}$ and FeMnCoCrNi at strains above 0.35. In the late stage of deformation ($\varepsilon > 0.35$), the stress of FeMnCoCrNi and $Fe_{50}Ni_{50}$ increases significantly with the increase of strain (Fig. 9b). Therefore, twinning and martensitic transformation jointly contribute to the stress elevation in these materials.

With the initial orientation of [123], the volume fraction of hcp-martensite in the HEA evolves more significantly than the low-entropy materials. In addition, more stacking faults are activated in FeMnCoCrNi and $Fe_{50}Ni_{50}$ compared with Cu, and the three materials show the similar activation of twinning. When the strain is between 0.1 and 0.28, FeMnCoCrNi and $Fe_{50}Ni_{50}$ show the much higher stress than Cu (Fig. 9c). Thus, the martensitic transformation in the HEA and the martensitic transformation, stacking faults, and twins in $Fe_{50}Ni_{50}$ contribute to their respective work hardening. Although hcp-martensite and twins also appear in the deformed Cu, twin boundary migration leads to the formation of slip steps on the free surfaces and thus the stress concentration within the sample (Fig. S6). The twin boundaries parallel to the fracture surfaces fail to prevent dislocation slip, which also leads to the rapid necking (Fig. 10i) and the continuously reduced stress of the model with deformation. Compared with experiments [6, 47, 50], stacking faults, deformation twins, and hcp-martensite are more likely to be formed in the studied alloys, which is attributed to the high strain rate applied in the MD simulations [58].

It is worth noting that in each single crystal the total atomic volume fractions of the three deformation structures, i.e., stacking faults, twin boundaries, and hcp-martensite, are equal to the volume fraction of the hcp structure (Fig. S5). For the [001] and [123] orientations, the activation capacities of these deformation mechanisms in the FeMnCoCrNi alloy are significantly higher than that in the low-entropy materials. This is consistent with the experimental observation that more twins are activated in the $Fe_{40}Mn_{40}Co_{10}Cr_{10}$ and the CoCrNi multi-principal-element alloys compared with conventional alloys, such as 316 stainless steel and

Fig. 11 Volume fraction evolution of stacking faults, twin boundaries, and hcp-martensite in the FeMnCoCrNi, Fe$_{50}$Ni$_{50}$, and Cu single crystals with different initial orientations. SF stacking fault; TWB twining boundary; HCP hcp-martensite

Hadfield steel [36, 37]. For the [110] orientation, at the initial stage of deformation ($\varepsilon < 0.1$) the total activation of stacking faults, twin boundaries, and hcp-martensite in FeMnCoCrNi is higher than that in Fe$_{50}$Ni$_{50}$ and Cu. With further deformation, the total activation of the above three deformation modes in the FeNi alloy is equal to and even exceeds that of the FeMnCoCrNi alloy. This is related to the more dislocation slip in the HEA with a larger lattice distortion (Fig. S4).

4 Conclusions

In this work, the orientation-dependent mechanical properties and plastic deformation mechanisms of the equiatomic FeMnCoCrNi HEA under uniaxial tensile loading have been studied systematically by atomistic simulations. The micromechanical behaviors of the HEA are also compared with

the low-entropy materials, i.e., Cu and Fe$_{50}$Ni$_{50}$. The main conclusions are as follows:

1. Significant dependence of mechanical properties on initial orientations is predicted in the HEA. For the studied orientations, the yield stress increases in the order: [001], [110], [123], [112], and [111]. In the plastic regime, the stress in each crystal decreases with increasing deformation except for the [123]-oriented HEA.
2. The activation of the orientation-dependent deformation modes is quantified by simulations. Plastic deformation of the FeMnCoCrNi HEA initially oriented with [001], [111], and [112] is dominated by stacking faults. The dislocation densities in those samples are higher than that in the [110] and [123] orientations. Stacking faults, twinning, and hcp-martensitic transformation jointly promote plastic deformation of the [110] orientation, and more twinning is activated in this sample compared with other orientations. The hcp-martensitic transfor-

mation is the dominant deformation mechanism in the [123] orientation, contributing to its good work hardening ability.

3. For the low-entropy materials, deformation twinning mainly contributes to the improved work hardening in both Cu and $Fe_{50}Ni_{50}$ alloys initially oriented with [001]. The [001]-oriented FeMnCoCrNi shows the higher dislocation density but the lower work hardening ability. When initially oriented with [110], only stacking faults and a small amount of twins are activated in Cu. The migration of twin boundaries leads to the non-uniform deformation, making its stress lower than that of the $Fe_{50}Ni_{50}$ and FeMnCoCrNi alloys with the same initial orientation at the strain above 0.35. Twins and hcp-martensite play a major role in the stress elevation of the $Fe_{50}Ni_{50}$ and FeMnCoCrNi alloys. For the [123] orientation, there are fewer stacking faults in Cu. In addition, neither hcp-martensite nor twins can prohibit necking caused by the migration of twin boundaries. This makes Cu deform inhomogeneously and facilitates the sample necking. In the $Fe_{50}Ni_{50}$ alloy, martensitic transformation, stacking faults, and twins jointly contribute to its higher strength. The formation of a large amount of hcp-martensite in the FeMnCoCrNi HEA majorly contributes to its good work hardening ability within the strain range of 0.1 and 0.28.

4. Compared with low-entropy materials, the larger lattice distortion in the HEA promotes more significant dislocation nucleation. Thus, the critical stress for the elastic–plastic transition of the HEA is lower than that of the low-entropy ones with the same orientations. Meanwhile, the HEA shows the remarkable capability of storing dislocations. However, for the FeMnCoCrNi HEA in which the deformation mode is relatively simple compared with the low-entropy crystals, e.g., the [001]-oriented sample, its high dislocation density and the extensively activated stacking faults are still not sufficient for strengthening the material.

References

[1] B. Cantor, I.T.H. Chang, P. Knight, A.J.B. Vincent, Mater. Sci. Eng. A **375–377**, 213 (2004)

[2] J.W. Yeh, S.K. Chen, S.J. Lin, J.Y. Gan, T.S. Chin, T.T. Shun, C.H. Tsau, S.Y. Chang, Adv. Eng. Mater. **6**, 299 (2004)

[3] H.Y. Diao, R. Feng, K.A. Dahmen, P.K. Liaw, Curr. Opin. Solid. State. Mater. Sci. **21**, 252 (2017)

[4] D.B. Miracle, O.N. Senkov, Acta Mater. **122**, 448 (2017)

[5] Z. Pei, Mater. Sci. Eng. A **737**, 132 (2018)

[6] B. Gludovatz, A. Hohenwarter, D. Catoor, E.H. Chang, E.P. George, R.O. Ritchie, Science **345**, 1153 (2014)

[7] S.H. Jiang, H. Wang, Y. Wu, X.J. Liu, H.H. Chen, M.J. Yao, B. Gault, D. Ponge, D. Raabe, A. Hirata, M.W. Chen, Y.D. Wang, Z.P. Lu, Nature **544**, 460 (2017)

[8] Z.M. Li, K.G. Pradeep, Y. Deng, D. Raabe, C.C. Tasan, Nature **534**, 227 (2016)

[9] Z. Lei, X. Liu, Y. Wu, H. Wang, S. Jiang, S. Wang, X. Hui, Y. Wu, B. Gault, P. Kontis, D. Raabe, L. Gu, Q. Zhang, H. Chen, H. Wang, J. Liu, K. An, Q. Zeng, T.G. Nieh, Z. Lu, Nature **563**, 546 (2018)

[10] Q. Ding, Y. Zhang, X. Chen, X. Fu, D. Chen, S. Chen, L. Gu, F. Wei, H. Bei, Y. Gao, M. Wen, J. Li, Z. Zhang, T. Zhu, R.O. Ritchie, Q. Yu, Nature **574**, 223 (2019)

[11] R. Zhang, S. Zhao, J. Ding, Y. Chong, T. Jia, C. Ophus, M. Asta, R.O. Ritchie, A.M. Minor, Nature **581**, 283 (2020)

[12] J.W. Yeh, J. Occup. Med. **65**, 1759 (2013)

[13] W.R. Zhang, P.K. Liaw, Y. Zhang, Sci. China Mater. **61**, 2 (2018)

[14] F. Tian, L.K. Varga, L. Vitos, Intermetallics **83**, 9 (2017)

[15] H. Ge, F. Tian, JOM **71**, 4225 (2019)

[16] S.S. Sohn, A.K. Silva, Y. Ikeda, F. Kormann, W. Lu, W.S. Choi, B. Gault, D. Ponge, J. Neugebauer, D. Raabe, Adv. Mater. **31**, 1807142 (2019)

[17] B. Yin, S. Yoshida, N. Tsuji, W.A. Curtin, Nat. Commun. **11**, 2507 (2020)

[18] F.H. Cao, Y.J. Wang, L.H. Dai, Acta Mater **194**, 283 (2020)

[19] H. Chang, T.W. Zhang, S.G. Ma, D. Zhao, R.L. Xiong, T. Wang, Z.Q. Li, Z.H. Wang, Mater. Des. **197**, 109202 (2021)

[20] P. Sathiyamoorthi, J. Moon, J.W. Bae, P. Asghari-Rad, H.S. Kim, Scr. Mater. **163**, 152 (2019)

[21] W. Fang, H. Yu, R. Chang, X. Zhang, P. Ji, B. Liu, J. Li, X. Qu, Y. Liu, F. Yin, Mater. Chem. Phys. **238**, 121897 (2019)

[22] Z. Li, D. Raabe, Mater. Chem. Phys. **210**, 29 (2018)

[23] Y. Bu, Z. Li, J. Liu, H. Wang, D. Raabe, W. Yang, Phys. Rev. Lett. **122**, 075502 (2019)

[24] M. Černý, J. Pokluda, Phys. Rev. B **82**, 174106 (2010)

[25] W. Lu, C.H. Liebscher, G. Dehm, D. Raabe, Z. Li, Adv. Mater. **30**, 1804727 (2018)

[26] L. Li, Z. Li, A.K. Silva, Z. Peng, H. Zhao, B. Gault, D. Raabe, Acta Mater. **178**, 1 (2019)

[27] W.M. Choi, Y.H. Jo, S.S. Sohn, S. Lee, B.J. Lee, N.P.J. Comput, Mater. **4**, 1 (2018)

[28] D. Ma, B. Grabowski, F. Körmann, J. Neugebauer, D. Raabe, Acta Mater. **100**, 90 (2015)

[29] H.F. Zhang, H.L. Yan, H. Yu, Z.W. Ji, Q.M. Hu, N. Jia, J. Mater. Sci. Technol. **48**, 146 (2020)

[30] D. Wei, X. Li, J. Jiang, W. Heng, Y. Koizumi, W.M. Choi, B.J. Lee, H.S. Kim, H. Kato, A. Chiba, Scr. Mater. **165**, 39 (2019)

[31] S. Huang, W. Li, S. Lu, F. Tian, J. Shen, E. Holmström, L. Vitos, Scr. Mater. **108**, 44 (2015)

[32] S. Huang, H. Huang, W. Li, D. Kim, S. Lu, X. Li, E. Holmstrom, S.K. Kwon, L. Vitos, Nat. Commun. **9**, 2381 (2018)

[33] A.J. Zaddach, C. Niu, C.C. Koch, D.L. Irving, JOM **65**, 1780 (2013)

34. W. Abuzaid, H. Sehitoglu, Mater. Charact. **129**, 288 (2017)

[35] L. Patriarca, A. Ojha, H. Sehitoglu, Y.I. Chumlyakov, Scr. Mater. **112**, 54 (2016)

[36] B. Uzer, S. Picak, J. Liu, T. Jozaghi, D. Canadinc, I. Karaman, Y.I. Chumlyakov, I. Kireeva, Mater. Res. Lett. **6**, 442 (2018)

[37] S. Picak, J. Liu, C. Hayrettin, W. Nasim, D. Canadinc, K. Xie, Y.I. Chumlyakov, I.V. Kireeva, I. Karaman, Acta Mater. **181**, 555 (2019)

[38] Q.J. Li, H. Sheng, E. Ma, Nat. Commun. **10**, 3563 (2019)

39. J. Li, Q. Fang, B. Liu, Y. Liu, Acta Mater. **147**, 35 (2018)

[40] G. Cheng, S. Yin, T.-H. Chang, G. Richter, H. Gao, Y. Zhu, Phys. Rev. Lett. **119**, 256101 (2017)

[41] Q. Fang, Y. Chen, J. Li, C. Jiang, B. Liu, Y. Liu, P.K. Liaw, Int. J. Plast. **114**, 161 (2019)

[42] S. Plimpton, J. Comput. Phys. **117**, 1 (1995)

[43] A. Stukowski, Modell. Simul. Mater. Sci. Eng. **18**, 015012 (2010)

[44] H. Tsuzuki, P.S. Branicio, J.P. Rino, Comput. Phys. Comm. **177**, 518 (2007)

[45] A. Stukowski, K. Albe, Modell. Simul. Mater. Sci. Eng. **18**, 085001 (2010)

[46] G.D. Sathiaraj, C.W. Tsai, J.W. Yeh, M. Jahazi, P.P. Bhattacharjee, J. Alloy. Compd. **688**, 752 (2016)

[47] M.F. Campos, S.A. Loureiro, D. Rodrigues, M.C.A. da Silva, N.B. de Lima, MSF **591–593**, 3 (2008)

[48] W. Li, S. Lu, Q.M. Hu, S.K. Kwon, B. Johansson, L. Votos, J. Phys.: Condens. Matter. **26**, 265005 (2014)

[49] A. Refaat Ali, S.A. Mahmoud, Z.M. Farid, K. Atef, Phys. Stat. Sol. A **165**, 377 (1998)

[50] X.B. Li, G.M. Jiang, J.P. Di, Y. Yang, C.L. Wang, Mater. Sci. Eng. A **772**, 138811 (2020)

[51] Y.M. Kim, B.J. Lee, Mater. Sci. Eng. A **733**, 449 (2007)

[52] Y.H. Zhang, Y. Zhuang, A. Hu, J.J. Kai, C.T. Liu, Scr. Mater. **130**, 96 (2017)

[53] H. Zhang, X. Sun, S. Lu, Z. Dong, X. Ding, Y. Wang, L. Vitos, Acta Mater. **155**, 12 (2018)

[54] M.A. Tschopp, D.L. McDowell, J. Mech. Phys. Solids **56**, 1806 (2008)

[55] I. Salehinia, D.F. Bahr, Int. J. Plast. **52**, 133 (2014)

[56] Z.J. Wang, Q.J. Li, Y. Li, L.C. Huang, L. Lu, M. Dao, J. Li, S. Suresh, Z.W. Shan, Nat. Commun. **8**, 1108 (2017)

[57] Y. Zhang, Y.J. Zhou, J.P. Lin, G.L. Chen, P.K. Liaw, Adv. Eng. Mater. **10**, 534 (2008)

[58] Y.T. Zhu, X.Z. Liao, X.L. Wu, Prog. Mater. Sci. **57**, 1 (2012)